

# 4 | AGN FLARES AS COUNTERPARTS TO LIGO/VIRGO MERGERS: NO CONFIDENT CAUSAL CONNECTION IN SPATIAL CORRELATION ANALYSIS

Work publicly available in **N. Veronesi**, S. van Velzen, E. M. Rossi  
<https://arxiv.org/pdf/2405.05318>, currently under review for publication on *Monthly Notices of the Royal Astronomical Society*, Reprinted here in its entirety.

## Abstract

The primary formation channel for the stellar-mass Binary Black Holes which have been detected merging by the LIGO-Virgo-KAGRA (LVK) collaboration is yet to be discerned. One of the main reason is that the detection of an Electromagnetic counterpart to such Gravitational Wave (GW) events, which could signpost their formation site, has so far been elusive. Recently, 20 Active Galactic Nuclei flaring activities detected by the Zwicky Transient Facility have been investigated as potential counterparts of GW events by Graham et al. (2023). We present the results of a spatial correlation analysis that involves such events and uses the up-to-date posterior samples of 78 mergers, detected during the third observing run of the LVK collaboration. We apply a likelihood method which takes into account the exact position of the flares within the 3D sky map of the GW events. We place an upper limit of 0.155 at a 90 per cent credibility level on the fraction of the detected coalescences that are physically related to an observed flare, whose posterior probability distribution peaks at a null value. Finally, we show that the typically larger values of the masses of the GW-events, which host at least one flare in their localisation volume, are also consistent with the no-connection hypothesis. This is because of a positive correlation between binary masses and the size of the localisation uncertainties.

## 4.1 Introduction

During the third observing run (O3) of the LIGO-Virgo-KAGRA (LVK) collaboration, Gravitational Waves (GWs) coming from 80 confirmed mergers of binaries of compact objects were detected (Abbott et al. 2023a, 2024). Several channels for the formation of the merging systems have been proposed (see Mapelli 2021, for a recent review). These pathways can be divided into two main categories: the evolution of isolated stellar binary systems, and the formation inside dense environments, such as Nuclear Star Clusters or accretion discs of Active Galactic Nuclei (AGN). The formation of merging Binary Black Holes (BBHs) in AGN discs is expected to be facilitated not only by the high density of compact objects, but also by their dynamical interaction with the gas (Stone et al. 2017; Li & Lai 2022, 2023a,b; Qian et al. 2024; Rowan et al. 2023, 2024; Rodríguez-Ramírez et al. 2024). For this reason, the so-called “AGN-channel” for the formation of merging binaries has been recently studied and modelled extensively.

The component masses of binaries coalescing in accretion discs around Massive Black Holes are expected to populate the high end of the astrophysical stellar-mass Black Hole mass spectrum presented in The LIGO Scientific Collaboration et al. (2021). This is mainly because Type I migration caused by the interaction between a gaseous disk and the compact objects within it makes mass segregation very efficient, since the migration time-scale is inversely proportional to the mass of the compact object (Armitage 2007; McKernan et al. 2011; Secunda et al. 2019). Migration can therefore increase the density of compact objects in the inner region of the AGN disc, where binary formation and hardening can be efficiently assisted by the interaction with the gaseous environment (Tagawa et al. 2020; Li et al. 2021, 2022b; DeLaurentiis et al. 2023a), unless it presents an elevated level of turbulence (Wu et al. 2024).

The vicinity to the central Massive Black Hole implies that mergers of compact objects inside an AGN accretion disc happen in the presence of a deep gravitational potential. For this reason, the speed at which the remnant objects get kicked from the location of the merger, typically of the order of hundreds of kilometres per second, is likely lower than the escape speed of the environment. Therefore there is the possibility for it to be retained and to take part to another BBH merger. In this scenario of hierarchical mergers, the components of the binaries are expected to have high masses and dimensionless spins close to  $\approx 0.7$ , which is the value that the remnant of a previous merger is expected to have, due to total angular momentum conservation (Gerosa & Berti 2017; Gerosa &

Fishbach 2021). In addition, binaries of compact objects merging inside an AGN disc have been modelled as able to develop and maintain a measurable level of eccentricity also in the LVK frequency range (Samsing et al. 2022; Calcino et al. 2023; Fabj & Samsing 2024). The detection of non-zero eccentricity in one or more GW signals would therefore represent a strong hint regarding the efficiency of disc-assisted BBH formation. Finally, the symmetry of an astrophysical environment such as a rotating disc has been claimed to be sufficient to explain the anti-correlation between the binary effective spin parameter  $\chi_{\text{eff}}$  and the mass ratio  $q$  that has been observed in the population of mergers detected by the LVK collaboration (McKernan et al. 2022a; Santini et al. 2023). The comparison of the binary parameters' distributions predicted for the AGN channel with the ones of detected GW events is a viable approach for estimating the fractional contribution of this formation path to the total BBH merger rate. For example, with this method Gayathri et al. (2023) estimated this fractional contribution to be approximately 20 per cent.

Alternatively, it is possible to put constraints on the this channel's efficiency by analysing the spatial correlation between the sky maps of the events detected by the LVK interferometers and the positions of observed AGN (Bartos et al. 2017a; Veronesi et al. 2022, 2023). In particular, in Veronesi et al. (2023) was found that the fraction of detected BBH mergers that took place in an AGN brighter than  $10^{45.5} \text{erg s}^{-1}$  ( $10^{46} \text{erg s}^{-1}$ ) is lower than 0.49 (0.17) at 95 per cent credibility level. This result tends to agree with the conclusions of the theoretical work presented in Grishin et al. (2024), where it is suggested that a reduced efficiency in creating over-densities of compact objects inside discs of luminous AGN is to be expected when taking into account prescriptions for Type I migration that are calibrated from 3D simulations (Jiménez & Masset 2017).

A third way to identify the host environment of the merging binaries is the direct detection of a transient Electromagnetic (EM) counterpart. The vast majority of the detected GW events are coalescences of BBHs, which are not generally expected to produce a detectable associated EM signal. However, such counterparts are expected to be produced, even if not necessarily detectable, whenever mergers take place in gaseous environments, like AGN accretion discs (Bartos 2016b; McKernan et al. 2019). A possible origin of these counterparts is Bondi accretion on the merging objects at a hyper-Eddington rate, that triggers a Bondi explosion (Wang et al. 2021d). Another potential source of a detectable EM transient is a jet coming from the accretion of magnetized medium onto the remnant object that traverses the gaseous disc after receiving a recoil kick from the merger event (Chen & Dai 2024). Recently, Graham et al. (2023, G23, here-

after) have identified 20 unusual AGN flaring activities observed by the Zwicky Transient Facility (ZTF; [Bellm et al. 2019](#); [Graham et al. 2019](#)) as potential EM counterparts of the GW events detected during O3. These transients have been labelled as not caused by Supernovae (SNe), Tidal Disruption Events (TDEs), or regular AGN variability. A possible physical cause of such flares is Bondi drag accretion and shock of the gas that interacts gravitationally with the kicked remnant of a merger event that happened inside the disc. The flare is expected to be manifest when such remnant reaches the  $\tau = 1$  optical depth surface of the disc. In [Tagawa et al. \(2024\)](#) is presented an emission model based on the presence of a Blandford-Znajek jet produced from BHs in AGN discs ([Tagawa et al. 2022, 2023](#)), and it is applied to the flares reported in G23, finding that such model can be consistent with the observed events after a number of assumptions were made, mainly regarding the accretion rate onto the stellar-mass BH, and the fraction of jet power that ends up in radiation.

In this work we present the results of a spatial and temporal correlation study for the identification of the host environment of the mergers detected by the LVK collaboration. In particular, this analysis focuses on the connection between the mergers detected during O3 and the 20 EM transients presented and examined in G23.

We calculate the posterior probability distribution of  $f_{\text{flare}}$ , the fraction of the LVK events detected during O3 that are causally connected to an AGN flare. We do this by using an adapted version of the statistical approach presented in [Veronesi et al. \(2023\)](#). This is a model-independent approach, we only take into account spatial and temporal correlation, but otherwise remain agnostic about which AGN and GW events are favorable counterparts.

In the past, Bayesian analyses have already been performed to investigate the spatial correlation between GW events and AGN flaring activities. In particular, the relation between the BBH merger GW190521 and a flare of the AGN J124942.3+344929, that had been proposed as a candidate EM counterpart by [Graham et al. \(2020\)](#), has been investigated by [Palmese et al. \(2021\)](#). Their spatial correlation analysis concluded that the match between the GW event and the EM transient has a probability of approximately 70 per cent of being caused by chance coincidence. The lack of a confident physical association between the same two events is also found by [Ashton et al. \(2021\)](#).

In Section 3.2 we present the properties of the data that have been used in the analysis, which include the GW detections and the AGN flares considered as potential EM counterparts. The description of the statistical method used to check the significance of the GW-AGN flares connection is in Section 2.2, while the results of its application to the observed data are presented in Section

**2.3.** Finally, in Section **2.4** we draw final conclusions from our results and discuss what are their implications concerning the physical relation between BBH mergers and AGN flares.

We adopt the cosmological parameters of the Cosmic Microwave Background observations by Planck (Planck Collaboration et al. 2016):  $H_0 = (67.8 \pm 0.9) \text{ km s}^{-1} \text{ Mpc}^{-1}$ ,  $\Omega_m = 0.308 \pm 0.012$ , and  $n_s = 0.968 \pm 0.006$ .

## 4.2 Datasets

In this section we first present the main properties of the AGN flares selected in G23 as potential EM counterparts to O3 detections. We then describe and list the GW events we use in our analysis. Finally we show all the spatial and temporal associations that exist between the two catalogues, both in the case of a 3D cross-match, and in the case of a 2D sky-projected one.

### 4.2.1 AGN flares

All the AGN flares we use in our analysis have been observed by ZTF. This facility uses a  $47\text{deg}^2$  field-of-view camera to cover the majority of the sky above a declination of  $-30^\circ$  every two or three nights in the g-band and in the r-band. To select potential EM counterparts for the GW events detected during O3, in G23 the data from the fifth release (DR5)<sup>1</sup> were used, and the search has been limited to AGN at a redshift  $z \leq 1.2$ , given the sensitivity the interferometers of LIGO and Virgo had during O3. The light curves of the observed AGN flares have been fitted with a Gaussian rise - exponential decay form (see Equation 13 in G23). From the original full sample were then removed all the flares that have been considered as originated from SNe, TDEs, or regular AGN variability. This selection has been done based on the timescales of the transients, their g-r colour, their rate of colour evolution, and their total observed energy. The resulting selected sample consists of 20 AGN flares that are considered as potential EM counterparts for the GW events detected during O3. All these flares have peaked during the time window that can allow a causal connection with at least one merger. This temporal match is considered possible if the AGN has not flared before the first GW detection or more than 200 days after the last one. Any merger happening after that time is not considered as a potential counterpart, since the estimated time required for the remnant of the merger to reach the edge of the accretion disc is of the order of tens of days.

<sup>1</sup><https://www.ztf.caltech.edu/page/dr5>

In Table 4.1 we list the main properties of the 20 potential counterparts. In particular we report the name of the AGN, the Right Ascension (RA) and Declination (Dec), the redshift, the Modified Julian Day (MJD) of the peak, and the Gaussian rise time of the light curve,  $t_g$ . The sky distribution of these transients is shown in Figure 4.1.

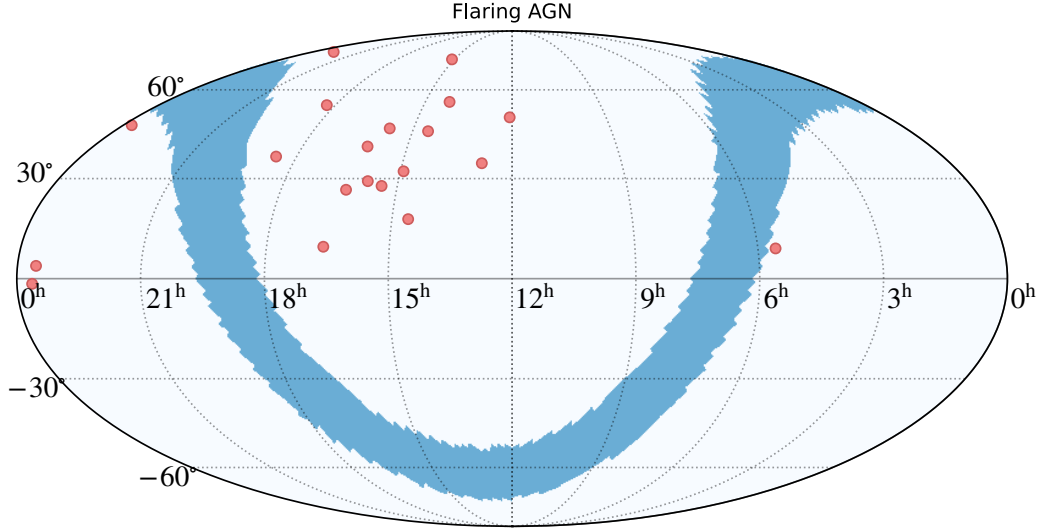


**Figure 4.1:** Mollweide projection of the sky position of the 20 AGN flare identified as potential EM counterparts of GW events in G23. The resolution corresponds to the one of an HealPix map with NSIDE=32. The pink markers correspond to the position of the flares, while the light blue region correspond to pixels that have a galactic latitude between  $-10^\circ$  and  $10^\circ$ . They correspond to the region that includes the galactic plane.

#### 4.2.2 GW events

We make use of 78 GW events detected during O3, which are contained in the Gravitational Wave Transient Catalog (GWTC) 2.1 (Abbott et al. 2024) and in GWTC 3 (Abbott et al. 2023a). The former includes all the events detected up to the first half of O3, O3a, started on April 1st, 2019 and ended on October 1st of the same year, while the latter includes all the events detected

**Table 4.1:** List of the 20 AGN flares that were selected in G23 as potential EM counterparts of GW events detected during O3. We report the name of the flaring object, its Right Ascension and Declination, its redshift, the MJD of the peak, and the Gaussian rise timescale. For J053408.41+085450.6 we use the same photometric estimate of the redshift that has been used in G23. For the AGN located at J150748.68+723506.1 and at J234420.76+471828.9 there is no available redshift estimate in the literature. These two sources are therefore excluded from the three-dimensional spatial correlation analysis presented in the following sections.

AGN name	RA [deg]	Dec [deg]	Redshift	MJD <sub>peak</sub>	$t_g$ [days]
J053408.42+085450.7	83.535	8.914	0.5*	58890	17
J120437.98+500024.0	181.158	50.007	0.389	58894	17
J124942.30+344928.9	192.426	34.825	0.438	58671	16
J140941.88+552928.1	212.425	55.491	0.074	58616	11
J143157.51+451544.0	217.990	45.262	0.693	58859	12
J143536.15+173755.4	218.901	17.362	0.095	58673	9
J145500.22+321637.1	223.751	32.277	0.177	58590	14
J150748.68+723506.1	226.953	72.585	—	58971	20
J152433.35+274311.6	231.139	27.720	0.069	58611	8
J154342.46+461233.4	235.927	46.209	0.599	58975	21
J154806.31+291216.3	237.026	29.205	1.090	58997	55
J160822.16+401217.8	242.092	40.205	0.627	58921	27
J161833.77+263226.0	244.641	26.541	0.126	58600	11
J163641.61+092459.2	249.173	9.416	1.155	58694	9
J181719.95+541910.0	274.333	54.319	0.234	58784	17
J183412.42+365655.2	278.552	36.949	0.419	58689	13
J224333.95+760619.2	340.891	76.105	0.353	58772	11
J233252.05+034559.7	353.217	3.767	1.119	58855	40
J233746.08-013116.3	354.442	-1.521	0.115	58703	8
J234420.76+471828.9	356.087	47.308	—	58669	11

during the second half of O3, O3b, that started on November 1st, 2019, and ended on March 27th, 2020. We only had to exclude GW200308\_173609 and GW200322\_091133 because for these two poorly-localized events the available data do not allow the evaluation of the size of the 90 per cent Credibility Level localisation volume (V90).

We work with the GW sky maps obtained from the latest (at the time in which this paper is written) versions of the posterior samples published by the Gravitational Wave Open Science Center (GWOSC) (Abbott et al. 2023b). Such samples were published on May 13th, 2022 for GWTC-2.1, and on June 23rd, 2023 for GWTC-3. Since G23 has been published in January 2023, we make use of a different, updated version of the posterior distributions for the events of GWTC-3, with respect to such work. The same is true for all the GW events for which in G23 GWTC-2.0 has been used. For such mergers, we use the posterior distributions of GWTC-2.1. The posterior samples coming from the IMRPHENOMXPHM (Pratten et al. 2021) waveform model have been used for every GW event a part from GW190425\_081805, GW191219\_163120, GW200105\_162426, and GW200115\_042309, for which the MIXED posterior samples were used.

To reproduce the analysis of GW23, we have to estimate the fraction of the 90 per cent credibility level localisation area (A90) that is outside the galactic plane and has been observed by ZTF at least 20 times in both the g-band and r-band in the 200 days following the LVK detection. This threshold number of observations is used to be consistent with G23. We call this parameter  $f_{\text{cover}}$ . To calculate it we use the ZTF forced photometry service (Masci et al. 2023) to obtain the number and the MJD of the observations at each sky location. The values of  $f_{\text{cover}}$  for all the sky maps we use in this work are listed in Table 4.4, together with the ID of the corresponding GW event, the catalogue it is contained in, the sizes of A90 and V90, and the MJD of the detection. The sizes of V90 we report refer to comoving localisation volumes, and not to Euclidean volumes in luminosity distance. This choice implies a cosmological model to be assumed during the cross-matching process, but leads to no difference in its results.

### 4.2.3 Matching events

The positions of the 20 flares listed in Table 4.1 are cross-matched with the sky maps of the GW events listed in Table 4.4. This is done using the `postprocess.crossmatch` function of the `ligo.skymap` package, searching space by descending probability density per unit comoving volume. The cross-matching



is performed both in the 3D comoving space, and in the 2D sky-projected space. For the 3D case, the two AGN flares without any redshift information are excluded. This is consistent with the approach used in G23, since these two potential counterparts are also not contained in their sample of 7 matching events.

To be considered as matching with a merger event, an AGN flare has to be found within the 90 per cent Credibility Level localisation volume (or area) of the sky map. Following GW23, we also require that the difference between the flare’s peak time and the GW detection time is smaller than 200 days and larger than the flare’s Gaussian rise time.

The 3D (2D) spatial and temporal cross-match of the 20 flares with the sky maps of the mergers detected during O3 finds that 11 (19) GW events and 8 (17) AGN flares match to yield a total of 12 (32) one-to-one matches. In other words, we find that for 12 (32) times one of the 8 (17) flares has peaked in one of the 11 (19) GW localisation volumes during the temporal window allowed for the match.

The one-to-one matches are listed in Table 4.2 and Table 4.3. For each of them we list the ID of the corresponding GW event, the name of the flaring AGN, and the credibility level corresponding to its position within the sky map of the merger.

### 4.3 Method

The goal of this work is to establish whether the matches between GW events and AGN flares that are listed in Table 4.2 and Table 4.3 are due to a causal connection or to random chance association. To do this, we calculate the posterior probability distribution of the parameter  $f_{\text{flare}}$ : i.e. of the fraction of detected mergers that have a causal connection with a flaring event. As examples of limiting outcomes, if our posterior would narrowly peak at  $f_{\text{flare}} = 0$  the chance association scenario would be highly favoured over the physical association scenario, and viceversa if the narrow peak would be at  $f_{\text{flare}} = 1$ .

We use an adapted version of the likelihood presented in Veronesi et al. (2023). Such function is based on the one described in Braun et al. (2008), which has been first re-adapted to investigate the spatial correlation between

**Table 4.2:** List of the 3D matches between GW events detected during O3 and AGN flares contained in ZTF DR5 and identified as potential EM counterparts. We report the ID of the GW event, the name of the flaring AGN, and the credibility level of its position within the localisation volume of the binary merger.

GW ID	AGN name	Credibility level
GW190514_065416	J224333.95+760619.2	0.175
GW190521_030229	J124942.30+344928.9	0.360
GW190620_030421	J124942.30+344928.9	0.778
GW190706_222641	J183412.42+365655.2	0.181
GW190708_232457	J233746.08-013116.3	0.839
GW190719_215514	J181719.95+541910.0	0.185
GW190731_140936	J053408.42+085450.7	0.479
GW190803_022701	J053408.42+085450.7	0.644
GW190803_022701	J120437.98+500024.0	0.543
GW200128_022011	J120437.98+500024.0	0.879
GW200216_220804	J154342.46+461233.4	0.727
GW200220_124850	J154342.46+461233.4	0.137

GW events and AGN in [Bartos et al. \(2017a\)](#). The general form is the following:

$$\begin{aligned}
\mathcal{L}(f_{\text{flare}}) &= \prod_{i=1}^{N_{\text{GW}}} \mathcal{L}_i(f_{\text{flare}}) \\
&= \prod_{i=1}^{N_{\text{GW}}} [f_{\text{cover},i} \cdot 0.90 \cdot f_{\text{flare}} \cdot \mathcal{S}_i + (1 - f_{\text{cover},i} \cdot 0.90 \cdot f_{\text{flare}}) \mathcal{B}_i], \quad (4.1)
\end{aligned}$$

where  $N_{\text{GW}}$  is the total number of GW detections. The value of  $f_{\text{cover},i}$  is used to weight the contribution of the  $i$ -th single-event likelihood function. For example, a GW event which sky map is characterised by  $f_{\text{cover}} = 0$  cannot contain any information regarding the connection with AGN flares observed by ZTF. Using  $f_{\text{cover},i}$  as weight in the likelihood calculation takes this into account. Analyses that investigate the spatial correlation between GW events and non-transient potential EM counterparts use as a weight for the single-event likelihoods the completeness of the AGN catalogue instead of  $f_{\text{cover},i}$  (see, for example [Veronesi et al. 2023](#)). The role of these parameters in these similar analyses is the same.

**Table 4.3:** List of the 2D sky-projected matches between GW events detected during O3 and AGN flares contained in ZTF DR5 and identified as potential EM counterparts. We report the ID of the GW event, the position of the flaring AGN name, and the credibility level of such position within the localisation area of the binary merger.

GW ID	AGN position	Credibility level
GW190425_081805	J124942.30+344928.9	0.750
GW190425_081805	J140941.88+552928.1	0.555
GW190425_081805	J152433.35+274311.6	0.281
GW190425_081805	J163641.61+092459.2	0.120
GW190514_065416	J224333.95+760619.2	0.479
GW190519_153144	J234420.76+471828.9	0.206
GW190521_030229	J124942.30+344928.9	0.640
GW190620_030421	J124942.30+344928.9	0.747
GW190620_030421	J143536.15+173755.4	0.893
GW190620_030421	J163641.61+092459.2	0.597
GW190706_222641	J183412.42+365655.2	0.685
GW190708_232457	J233252.05+034559.7	0.713
GW190708_232457	J233746.08-013116.3	0.626
GW190719_215514	J181719.95+541910.0	0.727
GW190731_140936	J053408.42+085450.7	0.379
GW190803_022701	J053408.42+085450.7	0.777
GW190803_022701	J120437.98+500024.0	0.544
GW190403_051529	J124942.30+344928.9	0.660
GW190403_051529	J140941.88+552928.1	0.856
GW191126_115259	J150748.68+723506.1	0.888
GW191129_134029	J154342.46+461233.4	0.895
GW191219_163120	J154342.46+461233.4	0.409
GW200105_162426	J053408.42+085450.7	0.790
GW200105_162426	J154342.46+461233.4	0.552
GW200105_162426	J154806.31+291216.3	0.369
GW200105_162426	J160822.16+401217.8	0.819
GW200112_155838	J154342.46+461233.4	0.839
GW200112_155838	J160822.16+401217.8	0.341
GW200210_092255	J154342.46+461233.4	0.836
GW200216_220804	J154342.46+461233.4	0.820
GW200216_220804	J154806.31+291216.3	0.890
GW200220_124850	J154342.46+461233.4	0.145

The signal probability density for the  $i$ -th GW event is calculated as follows:

$$\mathcal{S}_i = \sum_{j=1}^{N_{\text{matches}_i}} \frac{p_j}{n_{\text{flare},j}} \frac{1}{V90_i}, \quad (4.2)$$

where  $N_{\text{matches}_i}$  is the number of spatial and temporal matches the  $i$ -th GW event has with flares,  $p_j$  is the probability density associated to the position of the  $j$ -th matching EM transient, and  $n_{\text{flare},j}$  is the effective spatial number density correspondent to it. This number density is assumed to be uniform within V90.

In the analysis that involves the 2D sky-projected cross-match, A90 is used instead of V90, and both  $p_j$  and  $n_{\text{flare},j}$  are in units of  $\text{deg}^{-2}$ , and not in units of  $\text{Mpc}^{-3}$ . We calculate the effective number density as follows:

$$n_{\text{flare},j} = \frac{20}{V_{\text{ZTF,eff}}} \frac{200 - t_{\text{g},j}}{\Delta t_{\text{search}}}, \quad (4.3)$$

where 20 is the total number of AGN flares selected from ZTF DR5 as potential counterparts of GW events,  $V_{\text{ZTF,eff}} = 1.066 \times 10^{11} \text{Mpc}^3$  is the total effective surveyed comoving volume, and  $\Delta t_{\text{search}} = 562$  days is the total observing time of the search, between the start of O3 and 200 days after its end. We calculate the total effective comoving volume in order for it to be compatible with how  $f_{\text{cover}}$  has been calculated for each GW event, and to take into account the non uniformity of the source density in the ZTF footprint. We first map the sky into a HealPix grid with a resolution of NSIDE=32. To each pixel correspondent to a galactic latitude lower than  $-10^\circ$  or greater than  $10^\circ$  is then associated a number between 0 and 1. This value is the fraction of the total number of GW events for which that specific pixel was observed at least 20 times in both the ZTF g-band and r-band in the 200 days following the merger detection. These values are then all summed together and the result is multiplied by the angular size of each pixel. This sum corresponds to the total effective area observed by the survey during  $\Delta t_{\text{search}}$ ,  $A_{\text{ZTF,eff}}$ , and is used in the calculation of  $n_{\text{flare},j}$ , instead of  $V_{\text{ZTF,eff}}$ , in the case of the 2D sky-projected analysis. The value of  $V_{\text{ZTF,eff}}$  is finally calculated multiplying the total comoving volume enclosed within the redshift limit adopted in the search presented in G23,  $z = 1.2$ , by the ratio between  $A_{\text{ZTF,eff}}$  and the total area of the sky. Finally, the numerator of the second fraction in Equation 4.3 takes into account the width of the time window within which a specific flare has to peak in order to allow the match with a GW event. We calculate this quantity by subtracting the Gaussian rise

time of the flare from 200 days, the maximum allowed delay time between the peak of such EM transient and the GW detection.

The background probability density function  $\mathcal{B}_i$  is calculated in the same way as in Veronesi et al. (2023):

$$\mathcal{B}_i = \frac{0.9}{V90_i}, \quad (4.4)$$

where the 0.9 factor is used so that  $\mathcal{S}_i$  and  $\mathcal{B}_i$  are normalised to the same value. Just like the signal density function (Equation 4.2) A90 is used instead of V90 for the 2D cross-matching analysis.

Every single-event likelihood  $\mathcal{L}_i(f_{\text{flare}})$  is a monotonic function of  $f_{\text{flare}}$ , the only free parameter. For each merger, if  $\mathcal{S}_i > \mathcal{B}_i$ , then  $\mathcal{L}_i(f_{\text{flare}} = 1) > \mathcal{L}_i(f_{\text{flare}} = 0)$ ; this means that for that specific GW event our spatial correlation analysis favours the hypothesis according to which there is a causal connection with AGN flares. This can happen if there is an over-density of temporally-matching flaring activities inside the localisation volume of the merger, and/or if the potential counterparts are located in regions of the sky map with a high value of the probability density  $p_j$ . In general, the greater the difference between  $\mathcal{L}_i(f_{\text{flare}} = 1)$  and  $\mathcal{L}_i(f_{\text{flare}} = 0)$ , the more information the single-event likelihood brings to the total one.

The main distinction between the analysis presented in this work and previous ones, that involve cross-matching GW sky maps with regular AGN, is that flares are transient events. This is taken into account in different parts of our statistical framework. First and foremost, a temporal match is required between GW detections and observed AGN flaring activities in order for them to be considered as potentially related by causality. Moreover, each value of  $n_{\text{flare}}$  depends on the width of the temporal window that allows for a match, and on  $V_{\text{ZTF,eff}}$ . The latter takes into account the scanning pattern of ZTF and how much it covers the localisation areas of the mergers in the days after the detection. Finally, each value of  $f_{\text{cover}}$  accounts for transient nature of the potential EM counterparts considered in this work (see Section 4.2.2).

After normalising  $\mathcal{L}(f_{\text{flare}})$  using a flat prior on  $f_{\text{flare}}$  in the  $[0, 1]$  interval, we obtain the posterior distribution of this parameter.

## 4.4 Results

In this Section we present the posterior distribution of the fraction of detected GW events that have a connection with an AGN flare,  $f_{\text{flare}}$ . Then we show

the results of two more tests to check if this posterior is indeed compatible with the  $f_{\text{flare}} = 0$  hypothesis. The first of the two tests focuses the total number of matches between the catalogue of AGN flares and the one of GW events, the second on the binary mass distribution one should expect for the mergers characterised by at least one match.

#### 4.4.1 Posterior distributions

The posterior probability distribution on  $f_{\text{flare}}$  is estimated using the data presented in Section 3.2 and the method described in Section 2.2. The result is shown in Figure 4.2. For both the 3D and the 2D cross-matching analyses, the posterior distribution peaks at  $\hat{f}_{\text{flare}} = 0$ . In the case of the 3D analysis, the upper limits of the 68, 90, and 95 per cent Credibility Intervals (CIs) correspond to  $f_{\text{flare}} = 0.085$ ,  $f_{\text{flare}} = 0.155$ , and  $f_{\text{flare}} = 0.192$ , respectively. The upper limits for the same CIs in the 2D sky-projected analysis are  $f_{\text{flare}} = 0.056$ ,  $f_{\text{flare}} = 0.111$ , and  $f_{\text{flare}} = 0.142$ .

#### 4.4.2 Background Monte Carlo realisations

The posterior distributions presented in Section 4.4.1 peak at  $\hat{f}_{\text{flare}} = 0$ , which corresponds to the hypothesis of no causal connection between mergers detected by the LVK interferometers and the AGN flares selected as potential EM counterparts for such events. In other words, the positioning of the flares within the GW sky maps, and the observed number of matches between GW events and AGN flares appear consistent with chance associations only, without any physical relation between the two events.

To further test this hypothesis, we perform 500 Monte Carlo (MC) realisations of this background scenario. Each of them is constructed as follows:

- To generate a catalog of AGN flares that follows the ZTF real sampling of the sky, which is not fully uniform within the footprint, we sample 20 sky-positions from the catalogue of extra-galactic transient events presented in [van Velzen et al. \(2024\)](#);
- For each simulated flare, we select its peak time by drawing from the times its sky position was observed by ZTF. To match the peak time distribution of the 20 flares from G23, we require this peak time to be later than the start of O3 and earlier than the date that corresponds to 200 days after the end of the same observing run;

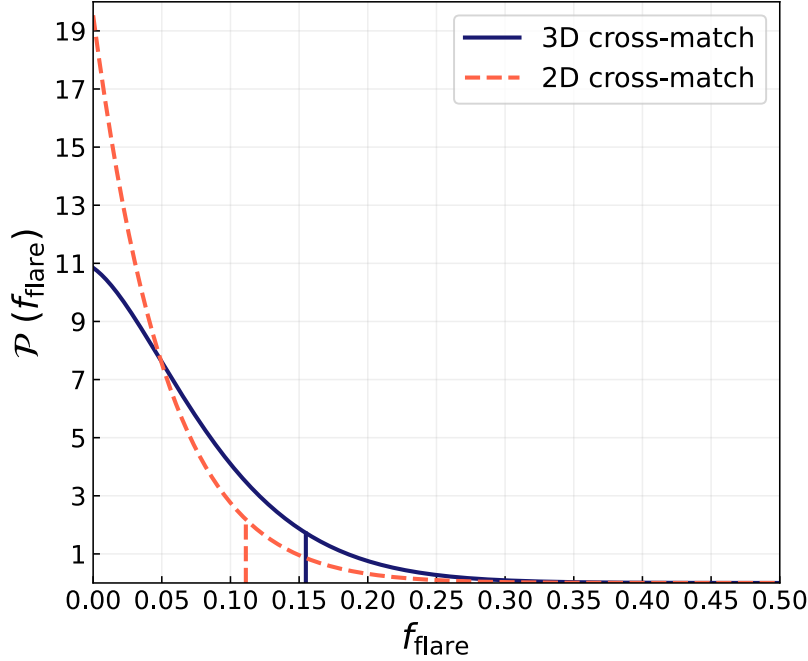


**Figure 4.2:** Posterior probability distribution on the fraction of GW events that are expected to have caused a flare in an AGN,  $f_{\text{flare}}$ . The solid blue line corresponds to the result of the 3D cross-matching analysis, while the dashed pink line to the one of the 2D sky-projected case. Both functions peak at  $\hat{f}_{\text{flare}} = 0$ . The vertical lines indicate the upper limits of the 90 per cent Credibility Intervals. These correspond to  $f_{\text{flare}} = 0.155$  and  $f_{\text{flare}} = 0.111$  for the 3D and 2D cross-matching analysis, respectively.

- To each of the 20 sampled positions we associate a value of redshift. This is obtained by inverse-sampling a linear interpolation of the Cumulative Distribution Function of the redshifts of the potential EM counterparts to GW events listed in Table 4.1;
- To each flare we associate a value for its rise time  $t_g$ , drawn randomly from the ones listed in Table 4.1;
- Once the catalogue of simulated background ZTF flares is constructed, it is cross-matched with the 3D sky maps of the GW events detected during O3 and listed in Table 4.4. As for the cross-match performed with observed data, in order for a match to be considered as valid, the flare has

to peak not more than 200 days after the GW detection, and not before that a number of days equal to the corresponding  $t_g$  have passed.

The histogram in Figure 4.3 shows the distribution of the number of spatial and temporal matches obtained in the 500 MC realisations of the background scenario. The average value of the sample is  $\bar{N}_{\text{matches}} = 14.9$  and its standard deviation is  $\sigma(N_{\text{matches}}) = 4.2$ . The number of matches obtained from observed data (12) is less than one standard deviation away from the mean of the distribution. It is reasonable then to assess that 12 matches can be expected even only due to random chance association.

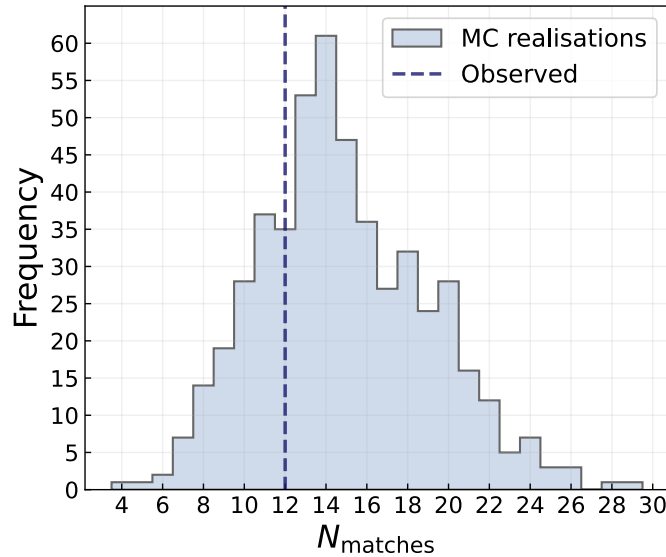


**Figure 4.3:** Distribution of the number of spatial and temporal matches between simulated ZTF AGN flares and GW 3D sky maps obtained from 500 MC realisations. Each of these realisations represents the scenario in which there is no causal connection between the two different signals, and every match is due to random chance association. The average of the distribution is  $\bar{N}_{\text{matches}} = 14.9$ , and its standard deviation is  $\sigma(N_{\text{matches}}) = 4.2$ . The vertical dashed line indicates the number of matches that have been found using real observed data (see Table 4.2).

For each MC realisation, the posterior distribution of  $f_{\text{flare}}$  is also obtained. In 150 realisations this function peaks at  $\hat{f}_{\text{flare}} = 0$ , and the distribution of the value of  $\hat{f}_{\text{flare}}$  extends to  $\hat{f}_{\text{flare}} \approx 0.26$ . This is similar to the posterior of  $f_{\text{flare}}$  obtained from observed data, again confirming that the outcome of our likelihood method (Eq.4.1) is consistent with the background hypothesis.



### 4.4.3 Binary Mass distributions

Due primarily to mass segregation and the possibility of undergoing subsequent hierarchical mergers, BBHs that coalesce inside dynamically dense environments like the accretion discs of an AGN are expected to have on average a higher mass with respect to the ones that formed through the evolution of an isolated binary stellar system. In Figure 4.4 it is shown the size of V90 for each GW event detected during O3, weighted by  $f_{\text{cover}}$ , as a function of the source-frame total mass of the merging binary. The horizontal and the vertical dashed lines indicate the median weighted size of V90 and the median total mass, respectively. The pink non-round markers indicate the 11 GW events that have at least one 3D match with a potential EM counterpart. We indeed notice that most of matching GW events have a total mass that is higher than the median. A KS test for the hypothesis that the mass distributions of the matching and the non-matching merging binaries are not related yields  $p = 0.018$ . However, this apparent difference in mass might be because the matching events are also associated with localisation uncertainties larger than the median. To test this hypothesis we follow the procedure presented hereunder:

- The average effective flare number density,  $\langle n_{\text{flare}} \rangle$ , is first calculated from Equation 4.3, using the average rise time of the flares listed in Table 4.1,  $\langle t_g \rangle = 17.35$ ;
- For all the GW events we evaluate the expected number of matches due to chance association,  $N_{\text{matches,exp}}$ , multiplying the size of their localisation volume by  $\langle n_{\text{flare}} \rangle$ ;
- We extract a number of matches for each GW event, drawing from a Poisson distribution with  $N_{\text{matches,exp}}$  as expectation value;
- We finally perform a two-sample Kolmogorov-Smirnov test between the distribution of the source-frame total mass of the GW events that have at least one match in this random sample and the distribution of the source-frame mass of the ones that don't have any match. For each repetition we therefore obtain a value of the KS statistic.

The whole process is repeated 10,000 times. The histogram in Figure 4.5 shows the distribution of the KS statistic for all the repetitions of the random sampling. We see that the KS statistic of the observed 11 matching GW events is consistent with the distribution obtained from the random sampling process. This means that the fact that the observed matching events correspond on average to higher

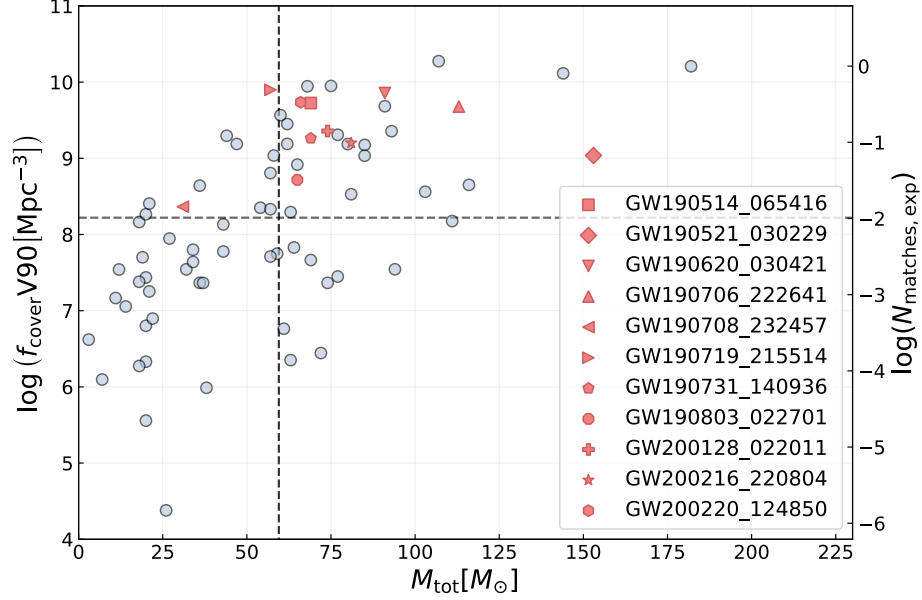


**Figure 4.4:** Effective size of V90 of the GW events detected during O3 as a function of the source-frame total mass of the binary. The 11 pink non-round markers indicate the mergers that have a spatial and temporal match with at least one of the AGN flares listed in Table 4.1. These matching sources appear to have a large mass compared to the median of the entire population (indicated with the dashed lines). However this can be explained by the correlation between mass and volume, see also Figure 4.5. On the right-hand side y-axis is indicated the expectation number of random matches evaluated assuming a uniform average effective number density calculated from Equation 4.3, using the mean  $t_g$  of the AGN flares.

binary masses with respect to the non-matching ones can be explained assuming random chance associations between GW sky maps and the AGN flares, if the positive correlation that exists between source-frame binary total masses and the size of the reconstruction volumes is taken into account.

## 4.5 Discussion and conclusion

We present a statistical investigation on the connection between the GW events detected during O3 and the AGN flares selected in G23 as potential EM counterparts. We do this using the most updated version of the posterior samples

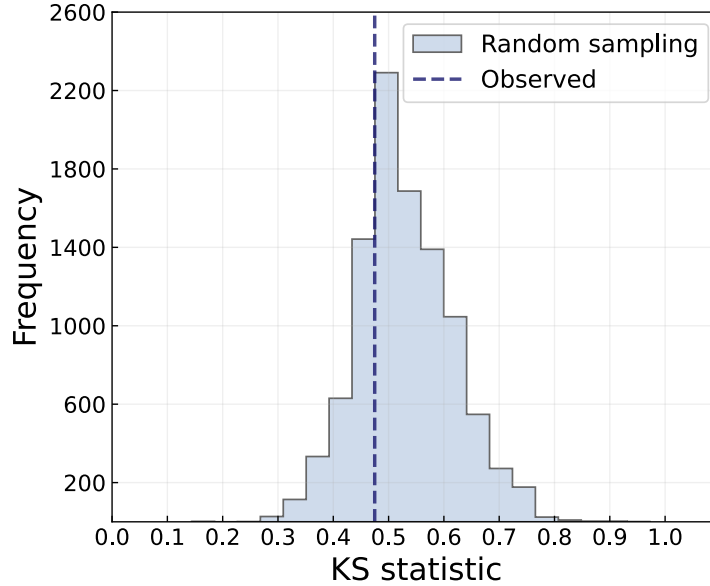


**Figure 4.5:** Distribution of the KS statistic obtained by comparing the source-frame total binary masses of GW events that have a 3D spatial match with an AGN flare with the ones of the other mergers detected during O3. The histogram shows the distribution of such statistic obtained from 10,000 repetitions of random sampling, where the number of matches of every GW event was drawn from a Poisson distribution that depends on the corresponding size of V90. The vertical dashed blue line indicates the value of the KS statistic calculated with the observed data. After correcting for the correlation between mass and V90, we thus find no evidence for a difference between the mass distribution of the GW sources that match to AGN flares and the mass distributions of the ones that do not.

released by the LVK collaboration. We make use of the statistical method presented in [Veronesi et al. \(2023\)](#) to estimate the posterior distribution over the fraction of GW events that have an observed AGN flare as an EM counterpart,  $f_{\text{flare}}$ . We repeat the same analysis both performing a 3D cross-match between the GW sky maps and the positions of the flares, and a 2D sky-projected one. In both cases the posterior distribution peaks at  $\hat{f}_{\text{flare}} = 0$ .

The upper limit of the 90 per cent CI is  $f_{\text{flare}} = 0.155$  in the case of the 3D cross-matching analysis and  $f_{\text{flare}} = 0.111$  for the 2D sky-projected case.

Moreover, we perform 500 MC realisations of the background hypothesis, according to which the matches between GW events and AGN flares are due

to random chance association. We find that the total number of matches that exist in the case of the real observed data (12) is compatible with this scenario.

Finally we find through a random sampling process, that the observed distribution of source-frame binary masses of the mergers that have a spatial and temporal match with at least one AGN flare is compatible with the same no-connection hypothesis.

We conclude that the hypothesis of no causal connection between the detected GW events and the observed AGN flares cannot be rejected.

In G23 Poisson statistic is used to calculate the probability of obtaining a number of matches equal or bigger than the observed one under the no causal connection hypothesis. They estimate this probability to be  $p = 0.0019$ . The estimate for the number of expected random matches used in G23 (2.83) is calculated assuming a spatial number density uniform in comoving volume up to  $z = 1.2$  and a temporal distribution of the flares over the whole duration of the data collection of ZTF DR5. This estimate is not compatible with the average number of matches we obtain in our Monte Carlo realisations of the background hypothesis (14.9). A key difference is that we take into account non-uniform distributions of the sky-position (by sampling from ZTF sources to obtain a realistic sky distributions) and redshift of the AGN flares (by sampling from the redshifts of the observed flares), and we allow these transient events to peak only in the time window that includes all the 20 selected potential counterparts. Below we explain this difference in more detail.

The main distinction between this work and G23 is that we measure a higher effective AGN flare number density, which leads to a higher expected number of matches under the background hypothesis. This difference is mainly driven by two factors. First, in G23 the fraction of matching temporal windows is calculated assuming a mean flare lifetime of 100 days and dividing it by 1000 days, approximately the duration of the observations of ZTF DR5. However, all the 20 AGN flares considered in the analysis peaked between the start of O3 and 200 days after its end, implying the effective duration of the ZTF flare search is 562 days. As such, we calculate for each flare the fraction of matching temporal windows by dividing the width of this window ( $200 \text{ days} - t_g$ ) by 562 days. This leads to a significant difference with respect to the value assumed in G23, since the average value of the rise times,  $t_g$ , is about 17 days. The second factor is a different estimate of the effective total comoving volume probed in the ZTF search. Our estimate ( $V_{\text{ZTF,eff}} = 1.066 \times 10^{11} \text{Mpc}^3$ ) takes into account the non-uniformity of the sky distribution of the ZTF extra-galactic sources and is approximately 1.5 times smaller compared to the ZTF volume used in G23. Taken together these two effects yield an effective source density that is

approximately 4.6 times larger than the one used in G23. We find a value of the total localisation volume weighted by  $f_{\text{cover}}$  similar to the ones used in G23, even using updated sky maps ( $1.457 \cdot 10^{11} \text{Mpc}^3$ , that corresponds approximately to 68 per cent of the value used in G23).

It is evident that our analysis only constraints the fraction of GW events in AGN that yield a detectable flare. Several factor can make this counterpart challenging to detect.

In order to produce a potentially observable flare not later than 200 days after the GW event, the recoil velocity has to be greater than a value that depends on the physical and geometrical characteristics of the AGN disc (see Equation 5 of G23). At the same time, an increase in the recoil velocity corresponds to a decrease in the Bondi-Hoyle-Lyttleton luminosity (see Equations 3 and 6 of G23). Therefore if the merger remnant travels too fast through the accretion disc, the hypothetical resulting flare will not be detected as it will not significantly exceed the luminosity of the host AGN. The recoil velocity of the merger remnant plays a role also in the jetted model of a BBH-induced AGN flare described in [Tagawa et al. \(2022\)](#) and in [Tagawa et al. \(2023\)](#). In particular, the rate at which the BH captures the gas, and therefore the luminosity of the jet, are expected to increase as a function of the velocity of such compact object with respect to the local motion of the disc (see Equation 1 of [Tagawa et al. 2022](#)). However, the accretion rate is expected to be reduced when the radius at which there can be gas accretion onto the BH on the timescale of the breakout of the jet at the surface of the AGN disc is much bigger than the radius at which the gaseous material remains bound to the compact object after the recoil kick. This is due to the ejection of gas beyond the bound region surrounding the merger remnant, and can happen if the recoil velocity is high ( $\gtrsim 2000 \text{ km s}^{-1}$  in the case of a BH with a mass of  $150 M_{\odot}$ ) (see Appendix B of [Tagawa et al. 2023](#), for a detailed description of the process).

On top of these physical factors regarding the observability of the flare caused by a kicked remnant exiting the accretion disc, there is a geometrical one. To be visible from instruments like ZTF, the flare has in fact to happen on the side of the disc that faces Earth, and on average this is expected to be true only in half of the cases.

Finally, in order to be confidently identified as a potential EM counterpart to a GW signal, the flare has to happen in a position in the sky that allows the light-curve to be scanned with several observations in different bands over its lifetime.

Current and future time-domain surveys such as ZTF and the Vera C. Rubin Observatory ([Ivezić et al. 2019](#)) are promising tools for the identification of

transient EM counterparts of GW events detected by the LVK collaboration. The low number density of transient EM events not compatible with regular AGN variability makes them ideal for spatial correlation analyses like the one presented in this work and for live searches of counterpart candidates of specific GW events, like the one presented in [Cabrer et al. \(2024\)](#), which focuses on the BBH merger candidate S230992g detected during the fourth observing run of the LVK collaboration.

Current data suggest that there is no correlation with events detected by the LVK interferometers, but updating the posterior distribution of  $f_{\text{flare}}$  with more data, or data more sensitive to lower amplitude flares, could yield better constraints on the relation between mergers of compact objects and AGN flares.

## Acknowledgements

The authors thank Matthew Graham for making the data of the 20 AGN flares mentioned in G23 available, and the anonymous referee, whose comments have helped to ameliorate the clarity of the presentation of our results. EMR acknowledges support from ERC Grant “VEGA P.”, number 101002511. This research has made use of data or software obtained from the Gravitational Wave Open Science Center ([gwosc.org](http://gwosc.org)), a service of LIGO Laboratory, the LIGO Scientific Collaboration, the Virgo Collaboration, and KAGRA. LIGO Laboratory and Advanced LIGO are funded by the United States National Science Foundation (NSF) as well as the Science and Technology Facilities Council (STFC) of the United Kingdom, the Max-Planck-Society (MPS), and the State of Niedersachsen/Germany for support of the construction of Advanced LIGO and construction and operation of the GEO600 detector. Additional support for Advanced LIGO was provided by the Australian Research Council. Virgo is funded, through the European Gravitational Observatory (EGO), by the French Centre National de Recherche Scientifique (CNRS), the Italian Istituto Nazionale di Fisica Nucleare (INFN) and the Dutch Nikhef, with contributions by institutions from Belgium, Germany, Greece, Hungary, Ireland, Japan, Monaco, Poland, Portugal, Spain. KAGRA is supported by Ministry of Education, Culture, Sports, Science and Technology (MEXT), Japan Society for the Promotion of Science (JSPS) in Japan; National Research Foundation (NRF) and Ministry of Science and ICT (MSIT) in Korea; Academia Sinica (AS) and National Science and Technology Council (NSTC) in Taiwan. *Software:* Numpy ([Harris et al. 2020](#)); Matplotlib ([Hunter 2007](#)); SciPy ([Virtanen et al. 2020](#)); Astropy ([Astropy Collaboration et al. 2013, 2018](#)); BAYESTAR ([Singer & Price 2016](#)).

## Data Availabilty

The data underlying this article will be shared on reasonable request to the corresponding author.

## Appendix: List of GW events

In Table 4.4 we list the properties of the GW events detected during O3 we used in the analysis presented in this work.

**Table 4.4:** List of GW events used in the analysis presented in this work. For each of them we list the ID, the catalogue it is contained in, the size of its 90 per cent credibility localisation area and volume, the Modified Julian Day of the detection, and the fraction of its 90 per cent credibility level localisation area that has been observed by ZTF at least 20 times in both the g-band and r-band during 200 days following the GW detection, at a galactic latitude  $|b| > 10^\circ$ .

GW ID	Catalogue	A90 [deg <sup>2</sup> ]	V90 [Mpc <sup>3</sup> ]	MJD	$f_{\text{cover}}$
GW190403_051519	GWTC-2.1	2731	$3.872 \cdot 10^{10}$	58576.2	0.487
GW190408_181802	GWTC-2.1	271	$8.922 \cdot 10^7$	58581.8	0.670
GW190412_053044	GWTC-2.1	25	$1.112 \cdot 10^6$	58585.2	0.875
GW190413_052954	GWTC-2.1	668	$2.017 \cdot 10^9$	58586.2	0.539
GW190413_134308	GWTC-2.1	562	$2.100 \cdot 10^9$	58586.6	0.161
GW190421_213856	GWTC-2.1	1237	$1.729 \cdot 10^9$	58594.9	0.013
GW190425_081805	GWTC-2.1	8728	$7.772 \cdot 10^6$	58598.3	0.537
GW190426_190642	GWTC-2.1	4559	$2.527 \cdot 10^{10}$	58599.8	0.638
GW190503_185404	GWTC-2.1	103	$4.716 \cdot 10^7$	58606.8	0.000
GW190512_180714	GWTC-2.1	274	$9.283 \cdot 10^7$	58615.8	0.250
GW190513_205428	GWTC-2.1	448	$3.805 \cdot 10^8$	58616.9	0.590
GW190514_065416	GWTC-2.1	3186	$1.063 \cdot 10^{10}$	58617.3	0.515
GW190517_055101	GWTC-2.1	365	$3.042 \cdot 10^8$	58620.2	0.222
GW190519_153544	GWTC-2.1	672	$1.180 \cdot 10^9$	58622.6	0.308
GW190521_030229	GWTC-2.1	1021	$3.434 \cdot 10^9$	58624.1	0.500
GW190521_074359	GWTC-2.1	469	$5.611 \cdot 10^7$	58624.3	0.500
GW190527_092055	GWTC-2.1	3640	$7.788 \cdot 10^9$	58630.4	0.473
GW190602_175927	GWTC-2.1	739	$1.412 \cdot 10^9$	58636.7	0.317
GW190620_030421	GWTC-2.1	6443	$1.219 \cdot 10^{10}$	58654.1	0.618

GW ID	catalogue	A90 [deg <sup>2</sup> ]	V90 [Mpc <sup>3</sup> ]	MJD	$f_{\text{cover}}$
GW190630_185205	GWTC-2.1	960	$1.104 \cdot 10^8$	58664.8	0.507
GW190701_203306	GWTC-2.1	43	$3.494 \cdot 10^7$	58665.9	1.000
GW190706_222641	GWTC-2.1	2596	$7.799 \cdot 10^9$	58670.9	0.590
GW190707_093326	GWTC-2.1	893	$6.443 \cdot 10^7$	58671.4	0.098
GW190708_232457	GWTC-2.1	11032	$9.846 \cdot 10^8$	58673.0	0.533
GW190719_215514	GWTC-2.1	3564	$1.317 \cdot 10^{10}$	58683.9	0.612
GW190720_000836	GWTC-2.1	35	$2.303 \cdot 10^6$	58684.0	0.000
GW190725_174728	GWTC-2.1	2142	$3.780 \cdot 10^8$	58689.7	0.386
GW190727_060333	GWTC-2.1	100	$1.963 \cdot 10^8$	58691.3	0.235
GW190728_064510	GWTC-2.1	321	$2.974 \cdot 10^7$	58692.3	0.602
GW190731_140936	GWTC-2.1	3532	$8.919 \cdot 10^9$	58695.6	0.357
GW190803_022701	GWTC-2.1	1012	$2.227 \cdot 10^9$	58698.1	0.684
GW190805_211137	GWTC-2.1	1538	$1.342 \cdot 10^{10}$	58700.9	0.664
GW190814_211039	GWTC-2.1	22	$3.590 \cdot 10^4$	58709.9	0.667
GW190828_063405	GWTC-2.1	340	$2.502 \cdot 10^8$	58723.3	0.205
GW190828_065509	GWTC-2.1	593	$2.700 \cdot 10^8$	58723.3	0.234
GW190910_112807	GWTC-2.1	8305	$5.158 \cdot 10^9$	58736.5	0.394
GW190915_235702	GWTC-2.1	432	$2.417 \cdot 10^8$	58742.0	0.889
GW190916_200658	GWTC-2.1	2368	$1.537 \cdot 10^{10}$	58742.8	0.574
GW190917_114630	GWTC-2.1	1687	$1.096 \cdot 10^8$	58743.5	0.317
GW190924_021846	GWTC-2.1	376	$1.209 \cdot 10^7$	58750.1	0.939
GW190925_232845	GWTC-2.1	876	$9.957 \cdot 10^7$	58752.0	0.232
GW190926_050336	GWTC-2.1	2015	$7.945 \cdot 10^9$	58752.2	0.355
GW190929_012149	GWTC-2.1	1651	$4.851 \cdot 10^9$	58755.1	0.468
GW190930_133541	GWTC-2.1	1493	$1.223 \cdot 10^8$	58756.6	0.223
GW191103_012549	GWTC-3	2171	$2.663 \cdot 10^8$	58790.1	0.692
GW191105_143521	GWTC-3	641	$1.250 \cdot 10^8$	58792.6	0.402
GW191109_010717	GWTC-3	1649	$4.863 \cdot 10^8$	58796.0	0.308
GW191113_071753	GWTC-3	2484	$1.159 \cdot 10^9$	58800.3	0.378
GW191126_115259	GWTC-3	1378	$5.990 \cdot 10^8$	58813.5	0.425
GW191127_050227	GWTC-3	983	$3.588 \cdot 10^9$	58814.2	0.418
GW191129_134029	GWTC-3	856	$5.496 \cdot 10^7$	58816.6	0.436
GW191204_110529	GWTC-3	3380	$3.436 \cdot 10^9$	58821.5	0.449
GW191204_171526	GWTC-3	256	$7.520 \cdot 10^6$	58821.7	0.284
GW191215_223052	GWTC-3	586	$4.535 \cdot 10^8$	58832.9	0.299
GW191216_213338	GWTC-3	206	$1.280 \cdot 10^6$	58833.9	0.282



GW ID	catalogue	A90 [deg <sup>2</sup> ]	V90 [Mpc <sup>3</sup> ]	MJD	$f_{\text{cover}}$
GW191219_163120	GWTC-3	2232	$7.504 \cdot 10^7$	58836.7	0.465
GW191222_033537	GWTC-3	2168	$3.687 \cdot 10^9$	58839.1	0.417
GW191230_180458	GWTC-3	1086	$4.376 \cdot 10^9$	58847.8	0.247
GW200105_162426	GWTC-3	7882	$3.345 \cdot 10^7$	58853.7	0.438
GW200112_155838	GWTC-3	3200	$5.599 \cdot 10^8$	58860.7	0.352
GW200115_042309	GWTC-3	512	$3.792 \cdot 10^6$	58863.2	0.329
GW200128_022011	GWTC-3	2415	$5.729 \cdot 10^9$	58876.1	0.357
GW200129_065458	GWTC-3	31	$2.617 \cdot 10^6$	58877.3	0.857
GW200202_154313	GWTC-3	150	$2.155 \cdot 10^6$	58881.7	0.872
GW200208_130117	GWTC-3	30	$3.075 \cdot 10^7$	58887.5	0.000
GW200208_222617	GWTC-3	2040	$1.214 \cdot 10^{10}$	58887.9	0.397
GW200209_085452	GWTC-3	877	$2.325 \cdot 10^9$	58888.4	0.664
GW200210_092255	GWTC-3	1387	$1.595 \cdot 10^8$	58889.4	0.555
GW200216_220804	GWTC-3	2924	$1.113 \cdot 10^{10}$	58895.9	0.750
GW200219_094415	GWTC-3	781	$1.902 \cdot 10^9$	58898.4	0.435
GW200220_061928	GWTC-3	4477	$4.333 \cdot 10^{10}$	58899.3	0.301
GW200220_124850	GWTC-3	3129	$1.185 \cdot 10^{10}$	58899.5	0.475
GW200224_222234	GWTC-3	42	$1.947 \cdot 10^7$	58903.9	0.143
GW200225_060421	GWTC-3	498	$8.177 \cdot 10^7$	58904.3	0.533
GW200302_015811	GWTC-3	6016	$2.778 \cdot 10^9$	58910.1	0.230
GW200306_093714	GWTC-3	3907	$4.302 \cdot 10^9$	58914.4	0.459
GW200311_115853	GWTC-3	35	$5.799 \cdot 10^6$	58919.5	1.000
GW200316_215756	GWTC-3	187	$3.634 \cdot 10^7$	58924.9	0.217